Advances in Water Resources 152 (2021) 103932

Contents lists available at ScienceDirect

Advances in Water Resources

journal homepage: www.elsevier.com/locate/advwatres

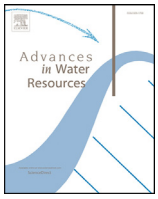

Image-based modeling of spontaneous imbibition in porous media by a dynamic pore network model

Chao-Zhong Qin[a,b,*], Harald van Brummelen[c], Mahmoud Hefny[d,e], Jianlin Zhao[f]

[a] State Key Laboratory of Coal Mine Disaster Dynamics and Control, Chongqing University, Chongqing, China
[b] School of Resources and Safety Engineering, Chongqing University, Chongqing, China
[c] Department of Mechanical Engineering, Eindhoven University of Technology, the Netherlands
[d] Geothermal Energy and Geofluids, Institute of Geophysics, ETH Zürich, Switzerland
[e] Geology Department, South Valley University, Egypt
[f] Department of Mechanical and Process Engineering, ETH Zürich, Switzerland

A B S T R A C T

The dynamic pore-network modeling, as an efficient pore-scale tool, has been used to understand imbibition in porous media, which plays an important role in many subsurface applications. In this work, we aim to develop a dynamic pore-network model for imaged-based modeling of spontaneous imbibition in porous media. The μCT scanning of a porous medium of sintered glass beads is selected as our study domain. We extract its pore network by using an open-source software of PoreSpy, and further project the extracted information of individual watersheds into multiform idealized pore elements. A number of case studies of primary spontaneous imbibition have been conducted by using both the pore-network model and a VOF model, under different wettability values and viscosity ratios. We compare those model predictions in terms of imbibition rates and temporal saturation profiles along the flow direction. We show that our pore-network model can well predict imbibition rates and temporal saturation profiles under different viscosity ratios and wetting conditions, in comparison to the VOF model. We explore the effect of viscosity ratio on the trapping of nonwetting phase. Moreover, we discuss the difference between spontaneous imbibition and quasi-static imbibition in terms of pore-filling mechanisms.

1. Introduction

Spontaneous imbibition plays an important role in many subsurface applications such as oil recovery in fractured reservoirs (Liu et al., 2020; Morrow and Mason, 2001), shale gas extraction (Zheng et al., 2018), and geological sequestration of carbon dioxide (Guo et al., 2016). In those applications, the imbibition rate and the trapping of nonwetting phase are of great interest. Spontaneous imbibition is usually categorized into cocurrent and countercurrent spontaneous imbibition. In cocurrent spontaneous imbibition, the wetting phase enters a porous medium through one boundary, while the nonwetting phase is displaced from the medium via other boundaries. By contrast, in countercurrent spontaneous imbibition, the wetting and nonwetting phases respectively enter and leave a porous medium via the same boundary. In this work, we focus on cocurrent spontaneous imbibition. Henceforth, spontaneous imbibition is referred to as cocurrent spontaneous imbibition, unless otherwise stated.

To predict the imbibition rate by the two-phase Darcy model, a number of material properties need to be determined such as capillary pressure and relative permeability (Alyafei et al., 2016; Schmid et al., 2016). Moreover, sharp wetting fronts observed in many core-scale experiments (Akin et al., 2000; Alyafei et al., 2016; Kuijpers et al., 2017) indicate that *dynamics* in spontaneous imbibition is strong, particularly at its early stage. This challenges conventional measurements of material properties which were mostly conducted in equilibrium or steady state (Zhuang et al., 2017). In this regard, pore-scale models of spontaneous imbibition are invaluable to explore the dynamic effect on those material properties. Furthermore, it helps to improve Darcy-scale imbibition models.

There have been extensive pore-scale numerical studies of two-phase flow in porous media, which cover a wide spectrum of research interests (Aker et al., 1998; Chen et al., 2020; Joekar-Niasar et al., 2010; Joekar-niasar and Hassanizadeh, 2012; Kunz et al., 2016; Qin, 2015; Raeini et al., 2015; Sweijen et al., 2016). In general, pore-scale models can be classified into first-principle models based on the Navier-Stokes equation, and pore-network models. First-principle models in porous media research are also called DNS (Direct Numerical Simulation) models. Popular DNS models include VOF (Volume of Fluid) model (Brackbill et al., 1992), LBM (Lattice-Boltzmann method) (Chen et al., 2014), SPH (Smoothed Particle Hydrodynamics) (Tartakovsky et al., 2016), and phase-field models (Shokrpour Roudbari et al., 2016; Yue and Feng, 2011). Although DNS models resolve complex porous structures directly, they are restricted by severe computational efforts. In addition, favorable contact angle values have been often used in simulations due to the deficiency of embedded contact line dynamics in DNS models. Alternatively, pore-network models first discretize

* Corresponding author.
E-mail address: chaozhong.qin@gmail.com (C.-Z. Qin).

https://doi.org/10.1016/j.advwatres.2021.103932
Received 31 January 2021; Received in revised form 19 April 2021; Accepted 24 April 2021
Available online 1 May 2021

complex pore structures into connected pore elements. Then, in conjunction with local rules, mass conversation of each phase is solved with the help of element-scale constitutive relations. In such way, pore-network models not only reduce computational efforts considerably, but also represent the pore-structure information adequately (Aghaei & Piri, 2015; Qin & van Brummelen, 2019). If dynamic effects can be neglected, pore-network models reduce to be quasi-static. Quasi-static pore-network models have been widely used in obtaining material properties such as relative permeability and capillary pressure (Patzek, 2001; Raeini et al., 2019). They have been widely used in the study of CO_2 trapping in the geological carbon storage (Valvatne and Blunt, 2004).

Up to now, dynamic pore-network models have been mostly used to qualitatively investigate fundamentals of two-phase flow in porous media (Huang et al., 2016; Joekar-Niasar et al., 2010; Li et al., 2017; Médici and Allen, 2013; Qin, 2015; Qin et al., 2019; Sheng and Thompson, 2016). Although a few imbibition models (Aghaei and Piri, 2015; Hughes and Blunt, 2000; Li et al., 2017; Nguyen et al., 2006; Sun et al., 2016; Tørå et al., 2012; Wang et al., 2015; Yang et al., 2017) under the constant-flux condition have been reported, either the used pore networks did not represent complex pore structures or the used local rules are not adequate to spontaneous imbibition. Verification studies of the dynamic pore-network modeling are scant in the open literature, because for a core plug (1) experimental data with high temporal resolution is difficult to obtain, and (2) oversimplified pore elements may not represent complex pore spaces. Recently, a verification of pore-scale models against experimental data of oil-water two-phase displacements in patterned microfluidics has been conducted (Zhao et al., 2019), which considered different wetting conditions under different injection rates of water (i.e., different capillary number values) (Zhao et al., 2016). The capabilities and limitations of their dynamic pore-network models were discussed in detail. However, for spontaneous imbibition, instead of a flux boundary condition, a pressure boundary condition is relevant. In principle, pore-scale events in spontaneous imbibition processes are different from those in drainage processes. Thus, a pore-network model for spontaneous imbibition requires specifically-defined local rules such as the competition of arc menisci (AMs) filling and main terminal meniscus (MTM) movement (Mason and Morrow, 1991).

We have developed a dynamic pore-network model specifically for spontaneous imbibition in porous media (Qin and van Brummelen, 2019). Multiform idealized pore elements have been used to represent complex pore structures so that our model bears the potential to quantitatively predict spontaneous imbibition in a 'real' porous medium. Preliminary case studies show that our model captures essentials of spontaneous imbibition such as imbibition rates and sharp wetting fronts (Gruener et al., 2012). In this work, we further develop the model to investigate spontaneous imbibition in a digital porous medium obtained by μCT. Moreover, as a first attempt, we compare our pore-network predictions with direct numerical simulations by the VOF model in terms of imbibition rates and temporal saturation profiles under different wettability values and viscosity ratios. Although direct numerical simulations are computationally heavy, they could provide us good references to study the efficient pore-network model (Raeini et al., 2015). To this end, we use a small piece of μCT scanning of sintered glass beads (Hoang et al., 2018), which resembles highly-permeable sandstones or carbonate rocks in terms of the complexity of pore spaces (Yang et al., 2019). In this work, we focus on the early stage of primary spontaneous imbibition in porous media where dynamics is strongest. In other words, the MTM move in a pore is predominant. PoreSpy (Gostick, 2017) is used to extract the pore-network information, which is properly projected into well-defined idealized pore elements. It is worth noting that the verification of VOF simulations or the pore-network modeling of spontaneous imbibition against experiments is excluded in this work, because benchmark data of spontaneous imbibition for the verification of pore-scale models are still absent in the open literature, to the best of our knowledge.

The remainder of the paper is structured as follows. In section 2, we introduce the dynamic pore-network model for spontaneous imbibition in porous media. In section 3, we present the used VOF model, which is implemented in the commercial solver FLUENT. A comprehensive comparison of pore-network modeling results and VOF results is given and discussed in section 4, which is followed by main conclusions in section 5.

2. Pore-network model

Our dynamic pore-network model comprises three elements: (1) a pore network representing the topology and the morphology of porous structures, (2) governing equations of mass conservation, and (3) constitutive relations assisted by local rules. The details of the pore-network model can be found in (Qin and van Brummelen, 2019). Here, we briefly present governing equations and key local rules. We focus on the pore-network extraction via PoreSpy (Gostick, 2017), and the preparation of the pore network to be used in the modeling.

2.1. Pore-network extraction

An open-source extraction code, PoreSpy, has been used to obtain the pore-network connectivity and geometric information of individual pores (Gostick, 2017). Watershed segmentation is used in the construction of pore bodies, while pore throats connecting pore bodies are volumeless (Rabbani et al., 2016). The key steps in the PoreSpy algorithm include (1) peak identification in the distance map, (2) removal of peaks on saddles and peaks which are too close to each other, and (3) watershed segmentation of pore spaces into pore bodies.

By PoreSpy we obtain the following pore-network information: (1) the connectivity map, (2) pore-body locations, inscribed and extended radii, and surface areas, and (3) pore-throat locations, inscribed and extended radii, perimeters, and cross-sectional areas. We project those information into idealized pore elements used in the dynamic pore-network model as follows. First, the inscribed radius in a pore body is equal to the inscribed radius of the corresponding watershed as $r_{pnm} = r_{ct}$, where the subscripts *pnm* and *ct* refer to the pore network and the original CT data respectively. Second, the pore-body length is approximated as $r_{ct} + R_{ct}$ where R_{ct} denotes the extended radius. Third, by virtue of volume conservation, the cross-sectional area of the pore body can be calculated as:

$$A_{pnm} = \frac{V_{ct}}{r_{ct} + R_{ct}} \tag{1}$$

where V_{ct} is the watershed volume. Fourth, together with r_{pnm}, the cross-sectional perimeter is given as (Patzek and Kristensen, 2001a):

$$P_{pnm} = \frac{2V_{ct}}{r_{ct}\left(r_{ct} + R_{ct}\right)} \tag{2}$$

Finally, the shape factor of the pore body is calculated according to $G_{pnm} = A_{pnm}/P_{pnm}^2$. Once the shape factor is known, an idealized pore body can be generated (Patzek and Kristensen, 2001a). We notice that surface areas cannot be directly projected due to the limitation of used idealized pore bodies. Although they would determine the flow resistance between neighbouring pore bodies, in this work we obtain the flow conductance of each pair of watersheds by the LBM modeling (Zhao et al., 2020a, 2020b). The shape factor of a pore throat is approximated as $G_{ij} = 0.5(G_i + G_j)$ where the subscripts *i* and *j* denote the pair of pore bodies.

The μCT image of sintered glass beads in the case studies has 200, 100, and 100 voxels along the X, Y, and Z directions, respectively. The voxel resolution is 25 μm. After segmentation, the pore voxels are shown in Fig. 1B. Fig. 1A shows the extracted pore network by PoreSpy, which has 346 pore bodies and 779 pore throats. Fig. 1C and D shows the pore-body and pore-throat size (i.e., the inscribed radius) distributions, and the shape-factor distribution of pore bodies.

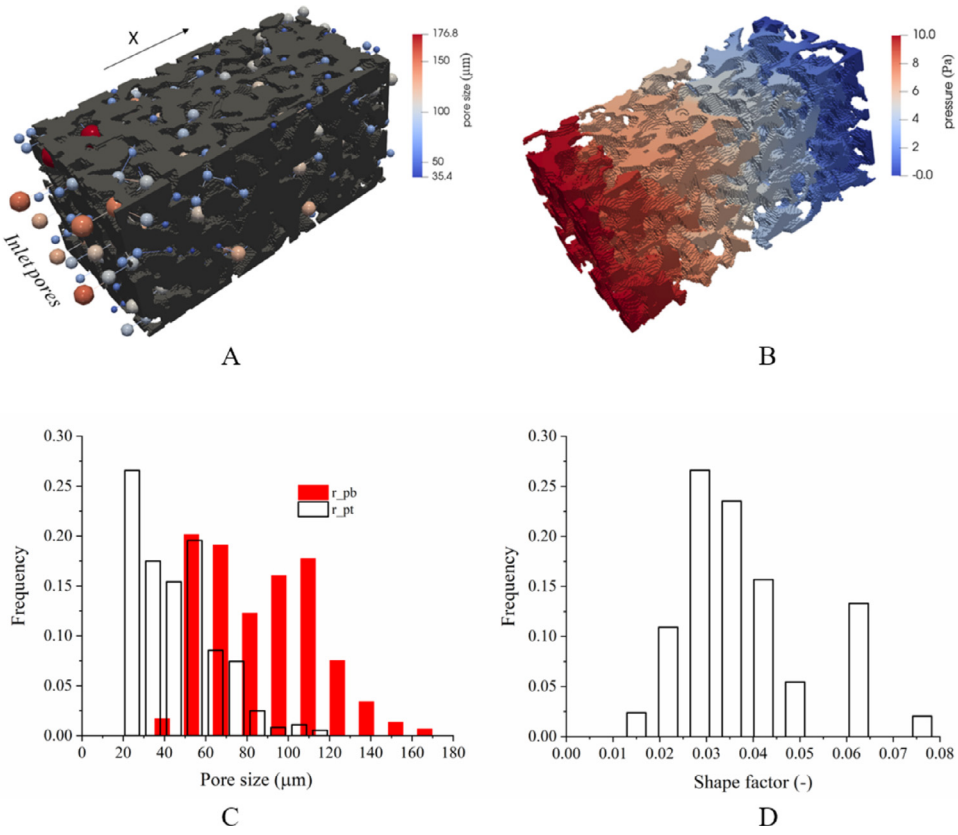

Fig. 1. (A) The pore network extracted by the open source software of PoreSpy. The color map shows the pore-body size (i.e., the inscribed radii of pore bodies). (B) The pore voxels of the μCT scanning of sintered glass beads. The color map shows the single-phase pressure. (C) The distributions of inscribed radii of pore bodies and pore throats. (D) The shape factor distribution of pore bodies.

Table 1
Geometrical and physical parameters used in the case studies.

μCT data	
Number of voxels in X, Y, and Z directions	200 × 100 × 100
Voxel resolution	25 μm
Porosity	0.27
Permeability by DNS	6.0×10^{-11} m^2
Pore network information	
Number of pore bodies and pore throats	346/779
Number of inlet and outlet pores	24/29
Porosity	0.27
Permeability	6.1×10^{-11} m^2
Mean pore size	97.3 μm
Physical parameters and model settings	
Water/air density	1000/1.2 kg/m^3
Water/air viscosity	1.0×10^{-3}/1.79×10^{-5} Pa s
Surface tension	0.073 N/m
Inlet/outlet pressure	0.0/0.0 Pa
Pre-wetting film capillary pressure	10^5 Pa

With pore-throat sizes from the PoreSpy, the calculated pore-network intrinsic permeability is 35 Darcy, which is around half of the DNS result (60 Darcy). This may indicate that the current network extraction needs to be improved (Gerke et al., 2020), or a new approach to parameterizing hydraulic conductance would be needed (Miao et al., 2017). As mentioned above, on the early stage of primary spontaneous imbibition, the MTM move is predominant, so that the imbibition rate would strongly depend on the intrinsic permeability. Therefore, we run LBM simulations of each pair of watersheds to obtain its single-phase conductance, and assign it to the corresponding pore throat (Zhao et al., 2020b). In this way, the pore-network intrinsic permeability is 61 Darcy, which is very close to the DNS result. The details of the μCT data and the pore-network information are given in Table 1.

2.2. Governing equations

By virtue of the incompressibility assumption, conservation of mass of the two phases translates into conservation of volume. The volumetric conservation of each phase is given as (Thompson, 2002):

$$V_i \frac{ds_i^\alpha}{dt} = -\sum_{j=1}^{N_i} K_{ij}^\alpha \left(p_i^\alpha - p_j^\alpha\right) \qquad \alpha = \{n, w\} \tag{3}$$

where i is the pore-body index, ij is the pore-throat index, n and w indicate the nonwetting and wetting phases, respectively, N_i is the coordination number of pore body i, V [m^3] is the volume, s [-] is the saturation, K [m^3/Pa/s] is the conductivity, and p [Pa] is the pressure. The gravity is neglected, since Bond number in our case studies is much smaller than 1.

With the definition of mixture pressure, $\bar{p} = p^n s^n + p^w s^w$, and adding the two conservation equations together (Eq. 3 for the wetting phase and for the nonwetting phase), the pressure equation is derived as (Joekar-Niasar et al., 2010):

$$\sum_{j=1}^{N_i} \left(K_{ij}^n + K_{ij}^w\right)\left(\bar{p}_i - \bar{p}_j\right) = -\sum_{j=1}^{N_i} \left\{ \left[K_{ij}^n s_i^w - K_{ij}^w \left(1 - s_i^w\right)\right] p_i^c + \left[K_{ij}^w \left(1 - s_j^w\right) - K_{ij}^n s_j^w\right] p_j^c \right\} \tag{4}$$

where the capillary pressure in pore body i is defined as $p^c = p^n - p^w$.

2.3. Local rules and constitutive relations

To consider a wide range of wetting conditions and real pore spaces, we have used capillary tubes of circular, square, and triangular cross-sections as our idealized pore elements (Qin and van Brummelen, 2019). Pioneering work has been done on the development of their local rules and constitutive relations (e.g., single-phase and two-phase conductance) (Blunt, 1997; Patzek, 2001; Patzek and Kristensen, 2001a, 2001b;

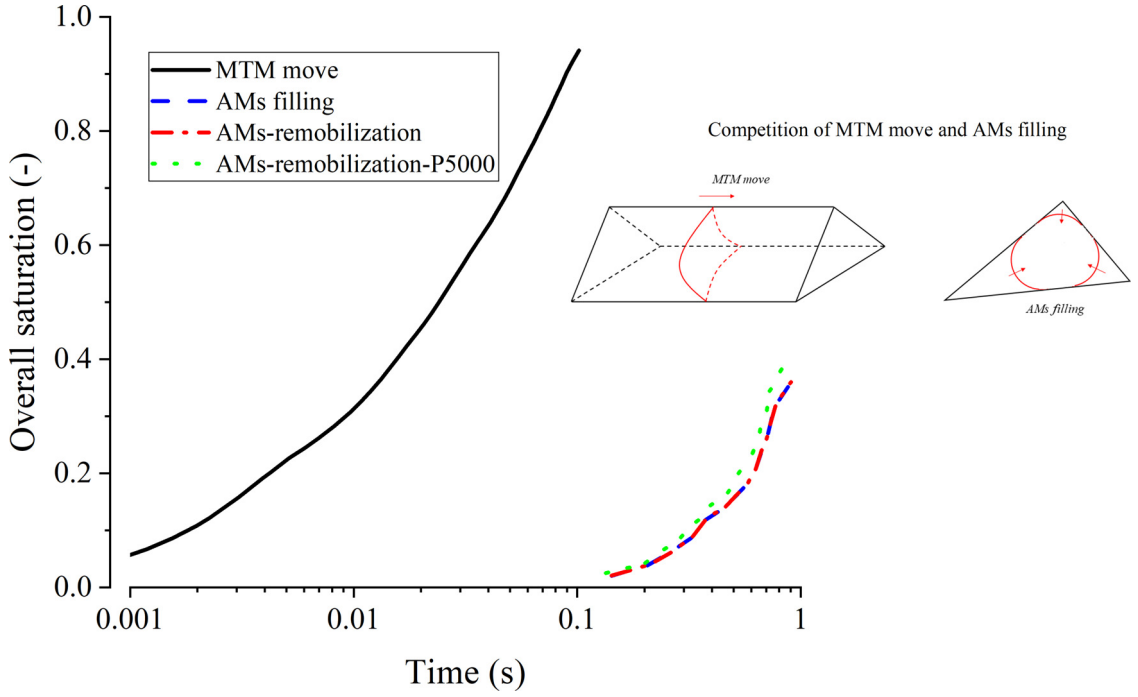

Fig. 2. Effect of local rules on the imbibition rate for the air-water system. The legend of 'AMs-remobilization-P5000' means the model uses the local rule of combining AMs filling and remobilization, as well as the inlet wetting pressure of 5000 Pa. The insert shows the schematic of the wetting-nonwetting interface move in a pore body: (Left) the MTM move, and (Right) the AMs filling.

Valvatne and Blunt, 2004). However, most previous studies have been focused on quasi-static displacements, to obtain two-phase material properties. We notice that, distinct from quasi-static displacements and dynamic drainage, spontaneous imbibition possesses a key feature of the competition of MTM move and AMs filling as shown by the insert in Fig. 2 (Mason and Morrow, 1991). Therefore, we cannot simply reverse a drainage process to simulate spontaneous imbibition. Instead, we should specifically develop local rules for facilitating the above-mentioned competition mechanism.

In our model development, the following local rules have been used. As shown in the flow chart in Fig. 3, first the wetting filling in a pore body is flagged as the MTM move, if one of the following three conditions is satisfied: (1) the AMs filling is unfavorable in the pore body; (2) any of its connected pore bodies is with the MTM move as well as its wetting saturation is larger than 0.5, and its capillary pressure is smaller than the MTM pressure of the pore body; (3) snap-off happens in any of its connected pore bodies, and its capillary pressure is smaller than the MTM pressure of the pore body. Second, when a pore body is with the MTM move, all of its pore throats are assumed to be wetting-filled. Meanwhile, the nonwetting is allowed to escape from the pore body. Third, when the MTM move is triggered in a pore body with the AMs filling, the wetting at corners instantaneously joins into the MTM. Fourth, when a pore body is with the MTM move, we assume single-phase conductance of both the wetting and nonwetting in the pore body. When the wetting saturation is close to 1.0 (e.g., 0.98 which is used in this work), we assume all of its connected pore throats are blocked to the nonwetting. Fifth, when the wetting saturation in a pore body is close to 1.0, we switch to a transition function of capillary pressure which forces capillary pressure to fast approach to the inlet wetting pressure (zero in spontaneous imbibition by default). Obviously, implementing the above local rules not only allows our dynamic pore-network model to simulate primary spontaneous imbibition of great interest, but also makes our model applicable to other imbibition conditions such as main imbibition and imbibition under a flux condition. It is worth noting that another proposed mechanism of remobilization of the nonwetting phase has been proposed in the modeling of spontaneous imbibition in a regular pore network with pore bodies of regular octahedron (Joekar-Niasar and Hassanizadeh, 2012). However, this mechanism at least has been proven to be not applicable to our idealized pore elements (i.e. capillary tubes with circular, square and triangular cross sections) (Patzek, 2001). Fig. 2 shows the effect of several local rules on the prediction of imbibition rate for the air-water system (water is the wetting). It is seen that the model drastically underestimates the imbibition rate and cause severe trapping of air, with the local rule of neglecting MTM move (i.e., sole AMs filling) or the local rule of combining AMs filling and remobilization.

Although we concentrate on spontaneous imbibition in an initially nonwetting-filled porous medium, in the model development we set a thin pre-wetting film at corners of a dry pore body when the wetting reaches any of its neighboring pore bodies. Additionally, the pore-throat capillary pressure is approximated by the smaller capillary pressure value of its two connected pore bodies.

The governing Eqs. (3, 4) are numerically solved for the primary variables: wetting saturation, s_i^w, and mixture pressure, $\bar{p}_i$. At the end of each time step, the remaining quantities such as capillary pressure and phase conductivity are updated based on the primary variables. The details of the calculation of constitutive relations of the used idealized pore elements are presented elsewhere (Qin and van Brummelen, 2019). For all case studies in this work, the mass imbalance of the wetting phase can be negligible, see Appendix C for the detail.

3. VOF (volume of fluid) model

Regarding direct numerical simulations of spontaneous imbibition, we use the VOF model to explicitly track interfaces between the nonwetting and wetting phases. Both phases are incompressible, and the flow is isothermal. In the VOF model, each computational cell is either one-phase or two-phase occupied. The phase fraction is defined as:

$$a^\alpha = \frac{V^\alpha}{V_{cell}} \qquad \alpha = \{n,\ w\} \tag{5}$$

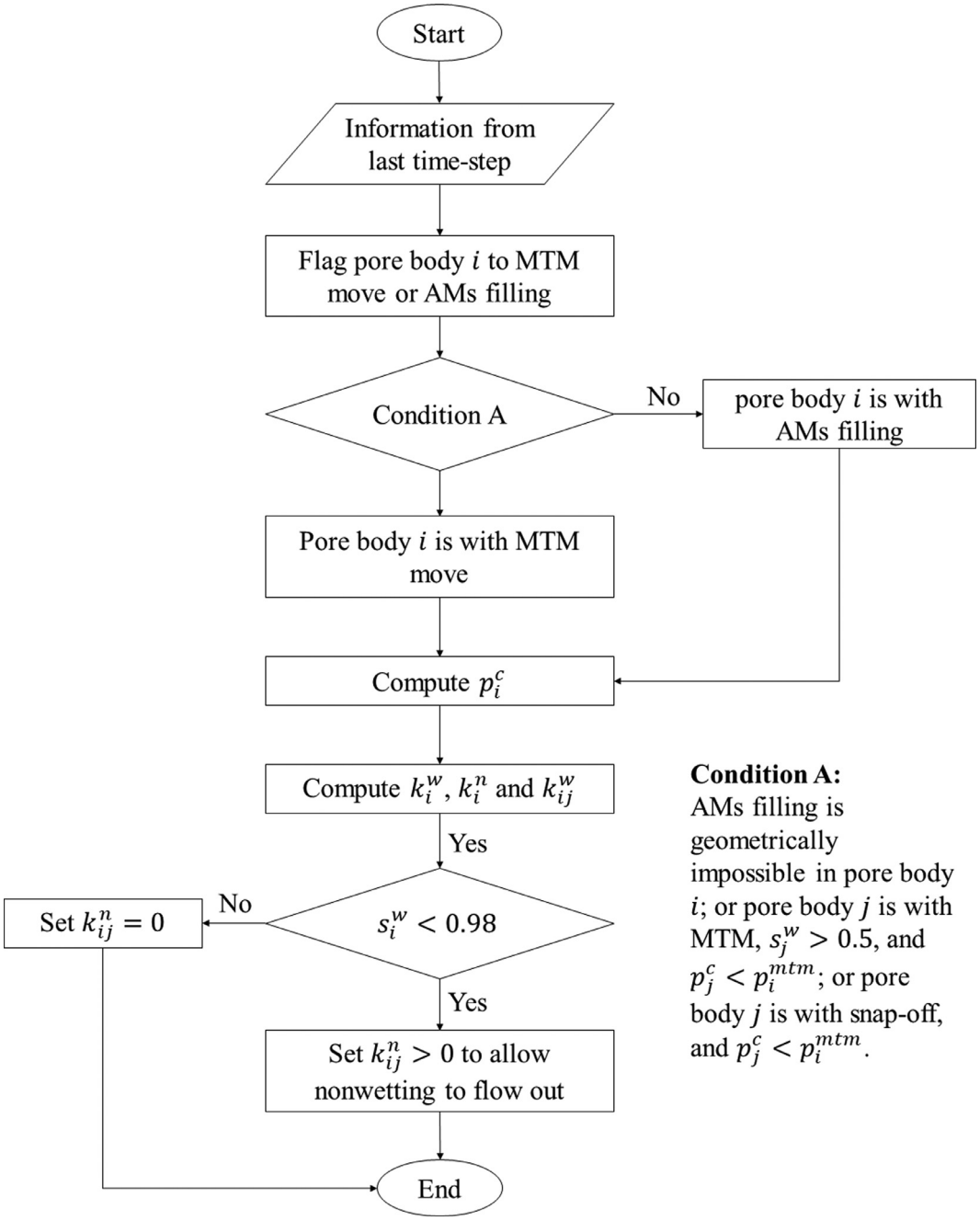

Fig. 3. Flow chart of the local rules for determining capillary pressure and phase conductance.

where α [-] is the phase indicator, V^α[m^3] is the volume of phase α in the computational cell, and V_{cell} is the volume of the computational cell. Neglecting the gravity, the governing equations of an isothermal, incompressible two-phase flow of Newtonian fluids are given as (Shams et al., 2018):

$$\nabla \cdot \mathbf{v} = 0 \tag{6}$$

$$\rho \frac{\partial \mathrm{v}}{\partial t} + \rho \mathbf{v} \cdot \nabla \mathbf{v} = -\nabla p + \mu \nabla^2 \mathbf{v} + \mathbf{F} \tag{7}$$

$$\frac{\partial a^w}{\partial t} + \nabla \cdot \left(a^w \mathrm{v}\right) = 0 \tag{8}$$

Here, ρ [kg/m^3] and μ [Pa s] are the mixture density and viscosity, respectively, which are defined as:

$$\rho = a^w \rho^w + \left(1 - a^w\right)\rho^n \tag{9}$$

$$\mu = a^w \mu^w + \left(1 - a^w\right)\mu^n \tag{10}$$

In Eq. 7, the source term, $\mathbf{F}$ [Pa/m], due to the addition of surface tension, is calculated by the continuum surface force (CSF) model (Brackbill et al., 1992) as:

$$\mathbf{F} = \sigma \frac{2\rho k \nabla a^w}{\rho^w + \rho^n} \tag{11}$$

where σ is the surface tension (N/m), and k [1/m] is the curvature of the nonwetting-wetting interface calculated by $\nabla \bullet (\nabla a^w / |\nabla a^w|)$.

To consider the wall adhesion, the meniscus normal in a two-phase occupied computational cell next to the wall is given as:

$$\mathrm{n} = \mathbf{n}^s \cos\theta + \mathbf{t}^s \sin\theta \tag{12}$$

where $\mathbf{n}^s$ and $\mathbf{t}^s$ are the unit vectors normal and tangential to the wall, respectively, and θ is the static contact angle.

The commercial solver FLUENT 17.2, which is (Finite Volume Method) FVM-based, is used to solve the governing Eqs. (6–8). The SIMPLE scheme is used to solve the Navier-Stokes Eqs. (6, 7). The second-order upwind scheme is used for the momentum discretization. Eq. 8 describes the transport of the volume fraction of wetting phase, which is a hyperbolic partial differential equation. Its discretization is crucial to VOF simulations. In this work, we use the geometric reconstruction scheme, which represents the nonwetting-wetting interface in a computational cell by a piecewise-linear approach (FLUENT 17.2 User's Guide).

For transient VOF simulations, the time step is crucial to numerical accuracy and computational cost. A large time step would give rise to smeared interfaces and even unreliable results, while a small time step entails huge computational efforts. To balance the two effects, we choose time steps such that the global Courant number is less than 0.5. For all simulated cases, in each time step, either the globally scaled residuals of all the equations are less than 10^{-6} or the maximum iteration number is over 50. The results show that before breakthrough of the wetting phase, the residual of 10^{-6} can be always reached.

The pore voxels of the μCT scanning as seen in Fig. 1B have been used as the computational cells in the VOF simulations. Since the mean pore size in radius is around 97.3 μm, this means that we have at least 8×8 cells of an average flow cross-section. Initially, the domain is saturated with the nonwetting phase (air or oil). The inlet pressure is set to zero, while the volume fraction of water is set to 1.0. The outlet pressure is set to zero, only allowing the nonwetting phase to flow back.

4. Results and discussion

A number of case studies of spontaneous imbibition in an initially nonwetting-filled porous medium are conducted by both the pore-network model and the VOF model, under different contact angle values and viscosity ratios. The used physical parameters and boundary conditions are given in Table 1. We compare the prediction results of pore-network modeling and VOF simulations in term of imbibition rates and temporal saturation profiles along the flow direction. We explore the effect of viscosity ratio on the trapping of nonwetting phase. Moreover, we discuss the difference between spontaneous imbibition and quasi-static imbibition in terms of pore-filling mechanisms. Regarding the mesh study and the verification of the used VOF model, one can refer to Appendix B for the detail. In summary, a mesh density with the voxel resolution of 25 μm is adequate for our VOF simulations of spontaneous imbibition in the μCT scanning of sintered glass beads. Similar mesh densities have been also reported in the VOF simulations of two-phase flow in porous media (Ferrari et al., 2015; Raeini et al., 2014).

4.1. Imbibition for the air-water system

Fig. 4 shows the imbibition rates under four different static contact angle values predicted by the VOF model. The wetting and nonwetting phases are water and air, respectively. It is seen that the VOF model predicts two almost overlapping imbibition curves for the contact angle values of 20° and 40°. There are two possible reasons for this observation: (1) the current mesh density cannot resolve highly curving interfaces, particularly when interfaces move through converging pore spaces, and (2) voxel-induced roughness impacts the wall adhesion model used in the VOF simulations. When the contact angle is set to 80° corresponding to a weakly water-wet medium, the imbibition front ceases near the inlet region as shown by the inset in Fig. 4. This is mainly due to diverging pore spaces which may locally flatten the nonwetting-wetting interfaces so that the imbibition driving force approaches to zero (Pavuluri et al., 2019). Furthermore, the CSF model (see Eq. 11) for calculating capillary forces may fail under extremely small capillary number values (Shams et al., 2018), which would numerically halt the wetting front movement. It is worth noting that experimental data show that the water imbibition front can continuously travel through porous materials

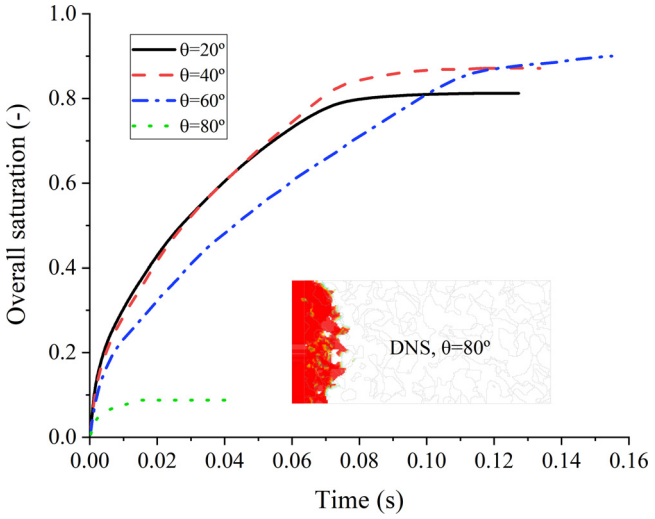

Fig. 4. Imbibition rates under four different static contact angle values predicted by the VOF model for the air-water system. The inset shows that the imbibition front stops at the inlet region under the static contact angle of 80°. The 'overall saturation' denotes the water saturation of the whole porous medium.

with the static contact angle even larger than 80° (Kuijpers et al., 2017). To sum up, for our case studies, the VOF model does not work well on the strongly or weakly water-wet porous medium which is represented by pore-space voxels. Therefore, in this work, we select VOF simulations with the contact angle values of 40° and 60° (corresponding to intermediately water-wet porous media) to compare with pore-network modeling results. Furthermore, in Appendix C, we show that for all case studies in this work, the capillary number values are smaller than 10^{-3}. This indicates that the dynamic effect on the contact angle is minor (Heshmati and Piri, 2014).

Fig. 5A shows the comparison of the imbibition rates predicted by the VOF model and the pore-network model, still for the air-water system. Two contact angle values of 40° and 60° are used. It is seen that the two model predictions match very well. The pore-network model has the big advantage of computational efficiency. It takes less than one minute for one case study running on a single core, while the VOF model needs a few days of 16-core parallel computation. Fig. 5B shows the comparison of the slope values predicted by the VOF model and the pore-network model. The slope value is calculated by $\Delta S/\Delta(\sqrt{t})$ where S denotes the overall saturation, and $\sqrt{t}$ is the square root of the imbibition time. It is seen that the two models predict close slope values as the overall saturation increases. From Fig. 5, however, we observe slight mismatch of the amount of trapped air in the end of the imbibition. This is because in the development of imbibition local rules, we set a maximum value of the wetting saturation of 0.98 in a pore body, above which all connected pore throats will be blocked of the nonwetting phase, while the VOF results show slightly less amount of trapped air. Nevertheless, this parameter does not impact the prediction of imbibition rates, and the trapping due to the connectivity/topology of pores.

Fig. 6A shows the water distributions in the porous medium under different overall saturation values predicted by the VOF model and the pore-network model. The nonwetting phase is air. The static contact angle is 40°. It is seen that the two models predict very close water distributions. As expected, a sharp wetting front propagates in the flow direction. The imbibition is predominated by the MTM move, along with minor corner fillings observed in the wetting front. Fig. 6B shows the corresponding water saturation profiles along the flow direction. For the pore-network modeling results, the cross-sectional saturation at each location is calculated by averaging a domain length of 500 μm, while for the VOF results, the cross-sectional saturation values are directly

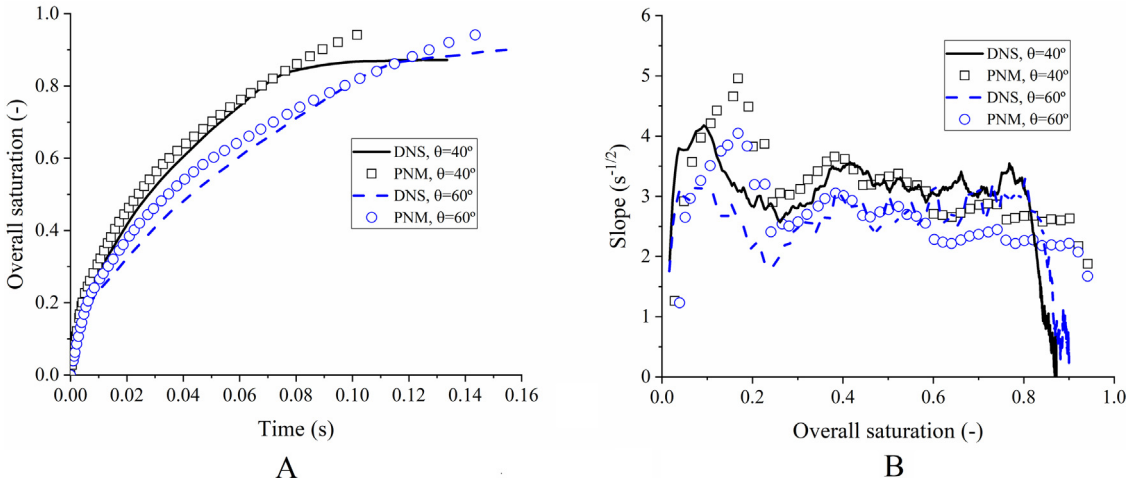

Fig. 5. (A) Comparison of the imbibition rates predicted by the VOF model and the pore-network model for the air-water system. Two contact angle values of 40° and 60° are used. (B) The corresponding slope values. The slope is calculated by $\Delta S/\Delta(\sqrt{t})$ where S denotes the overall saturation, and t is the imbibition time.

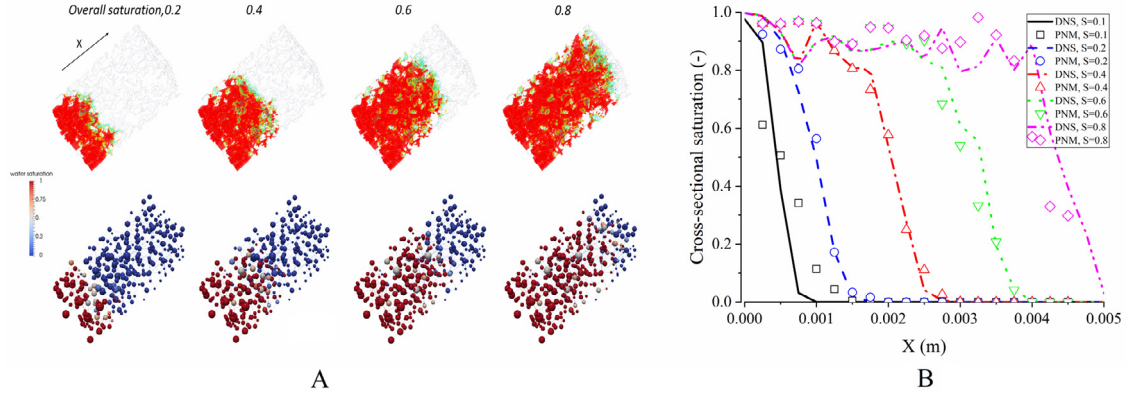

Fig. 6. (A) Water distributions in the porous domain under different overall saturation values predicted by the VOF model (upper row) and the pore-network model. In the upper row, the red color denotes the water phase, while the empty denotes air. The static contact angle is 40°. (B) The water saturation profiles along the flow direction. For the pore-network modeling results, the cross-sectional saturation at each location is calculated by averaging a domain length of 500 μm.

calculated at the same locations. It is found that the saturation profiles match each other at each overall saturation value.

4.2. Effect of viscosity ratio on imbibition

So far, we have shown that our dynamic pore-network model can adequately predict spontaneous imbibition in a complex porous medium, in comparison to VOF-based direct numerical simulations. In this subsection, we extend the comparison to cases with a more viscous nonwetting phase. Fig. 7A shows the comparison of the imbibition rates predicted by the VOF model and the pore-network model for the oil-water system. The viscosity ratio is assumed to be unity. The static contact angle is 60°. It is seen that the two model predictions match well. In comparison to the air-water system, oil is more viscous and much harder to be displaced so that the water front advances much slower. Fig. 7B shows the corresponding distributions of water saturation along the flow direction under different overall saturation values. The pore-network model predicts slightly rougher wetting fronts in comparison to those predicted by the VOF model. This discrepancy is partially due to that for the pore-network modeling results we calculate cross-sectional saturation values by averaging a domain length. Moreover, in the local rules (section 2.3), the assumption of nonwetting conductance in a pore body with the MTM move may deteriorate the prediction of wetting front, which is seen to be more pronounced in the case of a smaller viscosity ratio.

We further increase the viscosity of the nonwetting phase to 0.01 Pa s to test our dynamic pore-network model. Fig. 8A shows the comparison of the imbibition rates predicted by the VOF model and the pore-network model for the viscosity ratio of 0.1. Surprisingly, the imbibition rate predicted by the pore-network model matches well with that by the VOF model. Also, the saturation profiles are comparable as shown in Fig. 8B. In comparison to the saturation profiles under the viscosity ratios of 55.9 (i.e., the air-water system) and 1.0, the saturation profiles under the viscosity ratio of 0.1 are much spreading. In other words, the imbibition fronts are much rougher, which are in consistent with experimental observations (Akin et al., 2000).

From the above studies, we see that the viscosity ratio of the wetting to the nonwetting phases influences the roughness of wetting fronts. It further influences the trapping of the nonwetting phase. For the air-water system, the wetting phase itself depresses the roughness growth of the wetting front (Gruener et al., 2012), while much less viscous air does not play a role. Both experimental data (Akin et al., 2000; Kuijpers et al., 2017) and numerical results in this work show that a sharp wetting front advances through porous media. Moreover, a sharp wetting front is maintained over a long distance (Alyafei et al., 2016; Schmid et al., 2016) with little air trapped. As the increase of the nonwetting viscosity, wetting fronts in spontaneous imbibition become rougher and rougher. In principle, the nonwetting phase assists the roughness growth of the wetting front so that a diffusion-type wetting front is seen in the distributions of wetting saturation along the flow direction

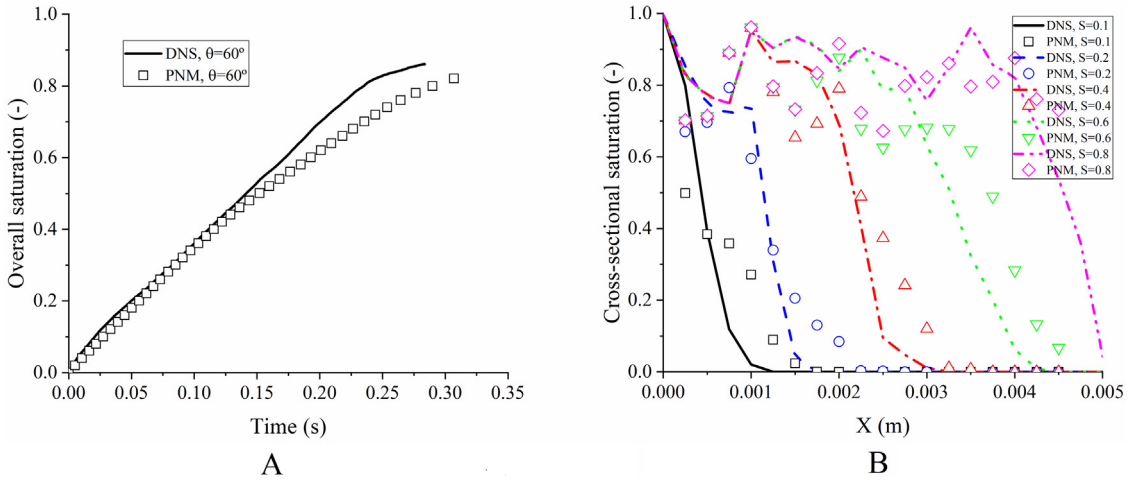

Fig. 7. (A) Comparison of the imbibition rates predicted by the VOF model and the pore-network model for the oil-water system. The oil viscosity is 1.0×10^{-3} Pa s. The contact angle is 60°. (B) The corresponding distributions of water saturation along the flow direction under different overall saturation values.

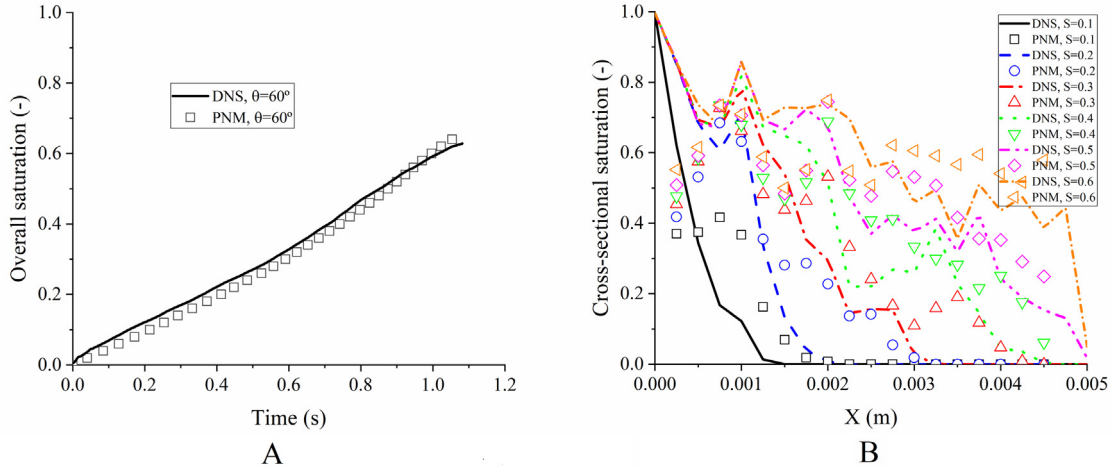

Fig. 8. (A) Comparison of the imbibition rates predicted by the VOF model and the pore-network model for a highly viscous nonwetting phase. The nonwetting viscosity is 0.01 Pa s. The contact angle is 60°. (B) The corresponding distributions of water saturation along the flow direction under different overall saturation values.

(Schembre and Kovscek, 1998; Vizika et al., 1994). Meanwhile, more and more nonwetting phase is trapped in the medium mainly due to the topology of pores. For instance, in the case of Fig. 8, around 40% of the nonwetting phase is trapped in the end of imbibition under the viscosity of 0.1.

Given the fact that the wetting phase flow deviates from the assumption of sing-phase regime, we would expect that the single-phase Darcy model is not applicable to a highly viscous nonwetting phase. To confirm this, we compare the Darcy predictions of imbibition rates with those by the pore-network model. The single-phase Darcy model for spontaneous imbibition is presented in Appendix A. The key assumption in the single-phase Darcy model is that a sharp wetting front holds in the imbibition process. The ordinary differential equation (Eq. A6) for the imbibition rate is numerically solved by Matlab. We use the effective mean pore size to approximate the REV-scale capillary pressure, which is estimated by $\tilde{R}^m = 1.2R^m$ by considering a mean shape factor of the pore bodies (Qin and van Brummelen, 2019). R^m is the mean pore size given in Table 1. The water saturation behind the wetting front is set to 0.9. Fig. 9 shows the comparison of the imbibition rates predicted by the VOF model and the single-phase Darcy model under different viscosity ratios. The contact angle is 60°. It is seen that the Darcy model well predicts the imbibition rate for the air-water system, even though the porous medium under study is smaller than

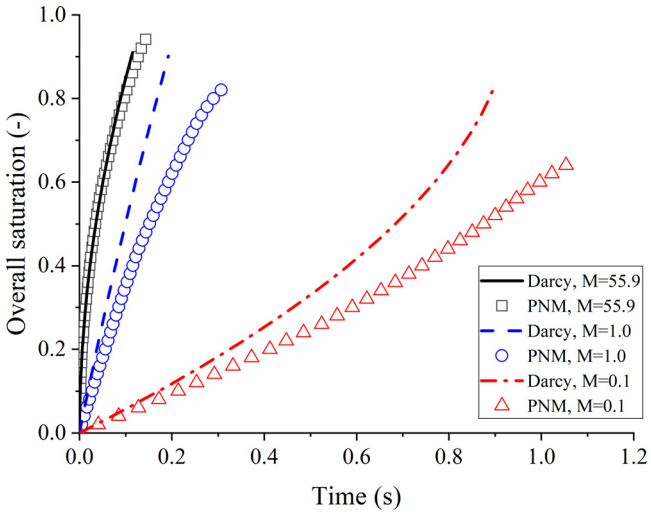

Fig. 9. Comparison of the imbibition rates predicted by the PNM model and the single-phase Darcy model (Eq. A6) under different viscosity ratios. The contact angle is 60°. The notation of 'Darcy, M=55.9' in the legend detonates the case study by the Darcy model under the viscosity ratio of 55.9 (i.e., the air-water system).

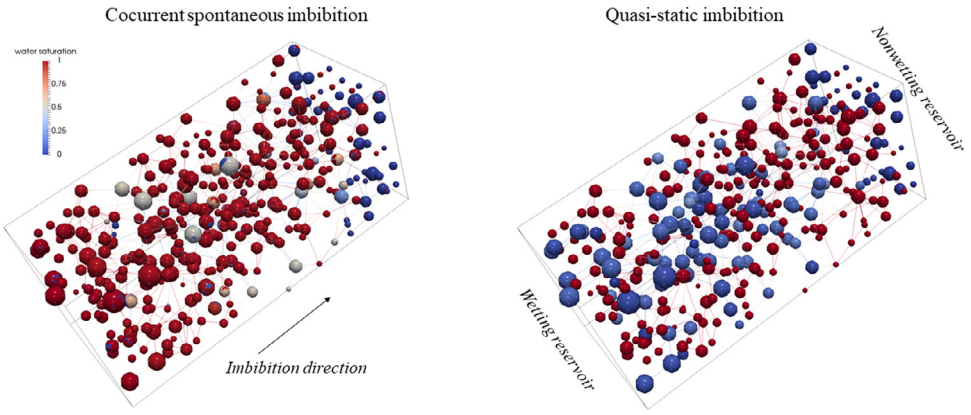

Fig. 10. Water distributions in the end of (Left) spontaneous and (Right) quasi-static imbibition for the air-water system. The contact angle is 40°.

its REV size. The predictions by the Darcy model, however, deviates from those by the pore-network model under the viscosity ratios of 1.0 and 0.1, which show faster imbibition. Obviously, this is mainly due to the failure of the assumption of a sharp wetting front. Moreover, it is seen that the discrepancy is larger in the case of the viscosity ratio of 0.1.

In the case of small viscosity ratios, and the case that the late stage of spontaneous imbibition is of interest (F. Zarandi and Pillai, 2018), the single-phase Darcy model will not be applicable any more. Then, one would resort to the two-phase Darcy model, in which capillary pressure and relative permeability curves are needed. To obtain two-phase material properties of spontaneous imbibition, the pore-scale modeling of a whole porous core up to several centimeters would be needed. In this context, an efficient and reliable pore-network model will be very useful, given the fact that DNS simulations are computationally prohibitive.

4.3. Comparison between spontaneous and quasi-static imbibition

The trapping of nonwetting phase is of great interest in a number of subsurface applications such as oil recovery and CO_2 storage. In practice, different imbibition conditions may be encountered such as cocurrent spontaneous imbibition, countercurrent spontaneous imbibition, and imbibition processes which are close to quasi-static. It is acknowledged that cocurrent spontaneous imbibition is fast, and its microscale dynamics is strong (Mason and Morrow, 2013). Here, with the help of our pore-network model, as a first attempt, we compare cocurrent spontaneous imbibition with quasi-static one, in terms of nonwetting-phase trapping and pore-filling mechanisms (i.e., the sequence of pore fillings). In the case of cocurrent spontaneous imbibition, we simulate the air-water system (i.e., the wicking process). The static contact angle is set to 40°. Regarding the quasi-static modeling, we use an in-house quasi-static pore-network code (Hefny et al., 2020), which considers key two-phase displacement mechanisms such as cooperative filling of pore bodies, piston-type move, and snap-off (Jackson et al., 2003; Patzek, 2001). We put the wetting reservoir at the inlet and the nonwetting reservoir at the outlet as shown in Fig. 10. We first run the primary drainage to the irreducible saturation of 0.05; then, we run the imbibition to the end (i.e., the nonwetting reservoir pressure reduces to zero).

Fig. 10 (Left) shows the water distribution in the end of spontaneous imbibition. It is seen that most pores are fully filled with water, with a few partially-filled large pores. The total amount of trapped air is only around 6%. This value is close to experimental data of a relatively homogeneous porous medium (Kuijpers et al., 2017). For the quasi-static imbibition in Fig. 10 (Right), as expected, water prefers to fill small pores, while much air is trapped in large pores. The resultant amount of trapped air is up to 48%, which is much higher than that in the spontaneous imbibition. The difference in the air trapping is because the two imbibition processes have different pore-filling mechanisms. In the spontaneous imbibition, we observe a co-filling mechanism between small and large pores, which results in a sharp wetting front. It is expected there will be less and less co-filling events as the increase of the nonwetting viscosity. In the quasi-static imbibition, however, the wetting filling shows a capillary-finger pattern. This is because in the absence of imbibition dynamics, the wetting filling follows the mechanism of percolation-invasion.

5. Conclusions

We have presented a dynamic pore-network model with specifically developed local rules for image-based modeling of spontaneous imbibition in porous media. A piece of μCT scanning of sintered glass beads is used as our porous domain. We have compared and verified our pore-network model against a widely used VOF model. A number of case studies of primary imbibition by both the pore-network model and the VOF model have been conducted, under different contact angle values and viscosity ratios. Based on those case studies, we arrive at the following main conclusions:

1 It is challenging for the VOF model to simulate spontaneous imbibition in a strongly or weakly water-wet porous medium, which is represented by pore-space voxels.
2 Our dynamic pore-network model can well predict imbibition rates and temporal saturation profiles along the flow direction under a wide range of viscosity ratios, in comparison to the VOF model.
3 For the air-water system, the wetting phase itself depresses the roughness growth of the wetting front. As the increase of the nonwetting viscosity, wetting fronts in spontaneous imbibition become rougher and rougher. Meanwhile, more and more nonwetting phase is trapped in large pores.
4 In spontaneous imbibition, we see a co-filling mechanism between small and large pores, which results in much less trapping of the nonwetting phase, in comparison to the quasi-static imbibition.
5 Our pore-network model is much more computationally efficient than the VOF model. The pore-network model running on a single core takes less than one minute for one case study, while the VOF model typically needs a few days of 16-core parallel computation.

Finally, we notice that a real sandstone or carbonate rock has distinct features of mixed-wettability, roughness of grain surfaces, and pore-scale heterogeneity, etc. Up to now, for a DNS model, it is still challenging to quantitatively predict their influence on two-phase flow dynamics. Therefore, the present pore-network model needs to be further improved and verified against lab experiments of spontaneous imbibition.

Declaration of Competing Interest

None.

Acknowledgment

C.Z.Q. acknowledges the support of National Natural Science Foundation of China (No. 12072053), the support of Human Resources and Social Security Bureau of Chongqing (No. cx2020087), and the support of Darcy Center of Utrecht University and Technology University of Eindhoven. This work is part of the research programme 'Fundamental Fluid Dynamic Challenges in Inkjet Printing' with project number FIP11, which is financed by the Dutch Research Council (NWO). The support of Océ Technologies within this program is acknowledged. The dataset associated with the present work is available via https://doi.org/10.6084/m9.figshare.10093676.

Appendix A

Spontaneous imbibition into a porous medium initially saturated with the nonwetting phase

By assuming a sharp wetting front, here we present the derivation of the 1D Darcy-scale model for spontaneous imbibition into a dry homogeneous porous medium as shown in Fig. A1. First, for the wetting phase, neglecting the gravity its Darcy flux is given as:

$$q^w = -\frac{k^w}{\mu^w}\frac{p^w}{l} \tag{A1}$$

where the superscript w denotes the wetting phase, q (m/s) is the flux, k (m^2) is the permeability, μ (Pa s) is the dynamic viscosity, l (m) is the wetting penetration length, and p (Pa) is the pressure. Then, we can write the rate of wetting saturation of the whole porous domain as follows:

$$AL\varepsilon\frac{dS}{dt} = -A\frac{k^w}{\mu^w}\frac{p^w}{l} \tag{A2}$$

where S is the wetting saturation of the whole porous domain, A is the cross-sectional area, L is the domain length, and ε is the porosity.

By virtue of volumetric conservation, and the condition of $p^n = p^c + p^w$ at the wetting front, we can write the nonwetting flux as:

$$q^n = q^w = \frac{k^n}{\mu^n}\frac{p^c + p^w}{L - l} \tag{A3}$$

Substitution of Eq. A1 into Eq. A3, and after some arithmetic manipulations, we can express the wetting phase pressure as:

$$p^w = -p^c \Big/ \left(1 + \frac{L-l}{l}\frac{k^w\mu^n}{k^n\mu^w}\right) \tag{A4}$$

Substitution of Eq. A4 into Eq. A2, we can obtain:

$$\frac{dS}{dt} = \frac{1}{L\varepsilon}\frac{k^w}{\mu^w}\frac{1}{l}\frac{p^c}{\left(1 + \frac{L-l}{l}\frac{k^w\mu^n}{k^n\mu^w}\right)} \tag{A5}$$

We assume a constant wetting saturation of S^f behind the wetting front so that the wetting penetration length can be expressed as $l = SL/S^f$. Further, the wetting permeability is approximated by $k^w = k^0 S^f$ where k^0 is the intrinsic permeability. Because the medium is initially nonwetting-saturated, the nonwetting permeability is given by $k^n = k^0$. Finally, the ordinary differential equation for the imbibition rate is written as:

$$\frac{dS}{dt} = \frac{S^f}{L^2\varepsilon S}\frac{k^0 S^f}{\mu^w}\frac{p^c}{\left(1 + \frac{S^f\mu^n}{\mu^w}\frac{S^f - S}{S}\right)} \tag{A6}$$

Appendix B

Test cases of spontaneous imbibition by the VOF model

We conduct case studies of spontaneous imbibition in simple capillary tubes, in order to understand the impact of mesh-density and mesh-type (i.e., conforming mesh and voxel mesh) on the predicted imbibition rate by the VOF model. Fig. B1-A shows the tube-scale saturation versus the imbibition time under four different contact angle values in a capillary tube of circular cross-section. The inset shows the used 'fine mesh'. This mesh has 19 elements along the diagonal and 36 elements along the circumference. Fig. B1-B shows the corresponding scaled imbibition slope values versus saturation. The imbibition slope is defined as $S/\sqrt{t}$, in which S is the tube-scale water saturation and t is the imbibition time. For each contact angle value θ, the scaling is $\sqrt{\cos 40^0/\cos\theta}$. It is seen that all curves collapse into the master curve of the contact angle value of 40°, except for some initial fluctuations due to the so-called inlet effect in DNS simulations (Yin et al., 2019). In Fig. B1-C, we decrease the mesh-density by 2, and compare the predicted imbibition rates, which are also compared with that by the LW equation (i.e., $S = \sqrt{r\sigma\cos\theta/(2\mu L^2)}$, in which r is the radius, σ is the surface tension, μ is the water dynamic viscosity, and L is the tube length). The differences in the imbibition rates predicted by the VOF model with a fine mesh and a coarse mesh are negligible. In addition, the imbibition rates predicted by the VOF model match with that of the LW equation. For spontaneous imbibition in a capillary tube of triangular cross-section, as shown in Fig. B1-D, the predicted imbibition rate of the coarse mesh is slightly larger than that under the fine mesh. However, both results match well with that of the LW equation. Notice that in the calculation of imbibition rate by the LW equation for the capillary tube of right triangular cross-section, the entry pressure (i.e., the capillary pressure) is calculated by the MS-P theory (Mayer and Stowe, 1965; Princen, 1970).

We further study the impact of mesh-type and mesh-refinement on the imbibition rate for a single 2D curved capillary tube. The left graph in Fig. B2 shows the voxel-representation and smooth-geometry representation of the half of a 2D capillary tube. The wall-boundary length of the voxel-representation (due to voxel-induced roughness) is longer than that of the smooth representation by 27%. The computational domain includes the wetting reservoir and the converging and diverging tube. The radius of the tube throat and the radius of the outlet are 20 μm and 80 μm, respectively. The length of the tube is 150 μm. Initially the tube is saturated with air; then water imbibes in. The right graph of Fig. B2 shows the imbibition rates under different mesh types and

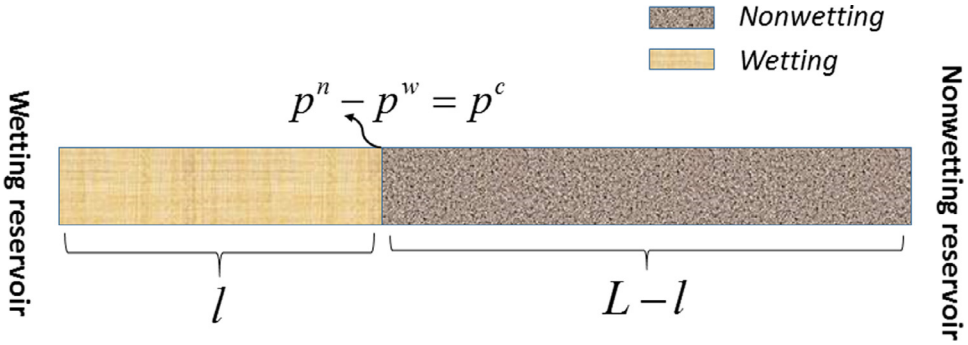

Fig. A1. Schematic of spontaneous imbibition into a dry porous medium at the Darcy scale.

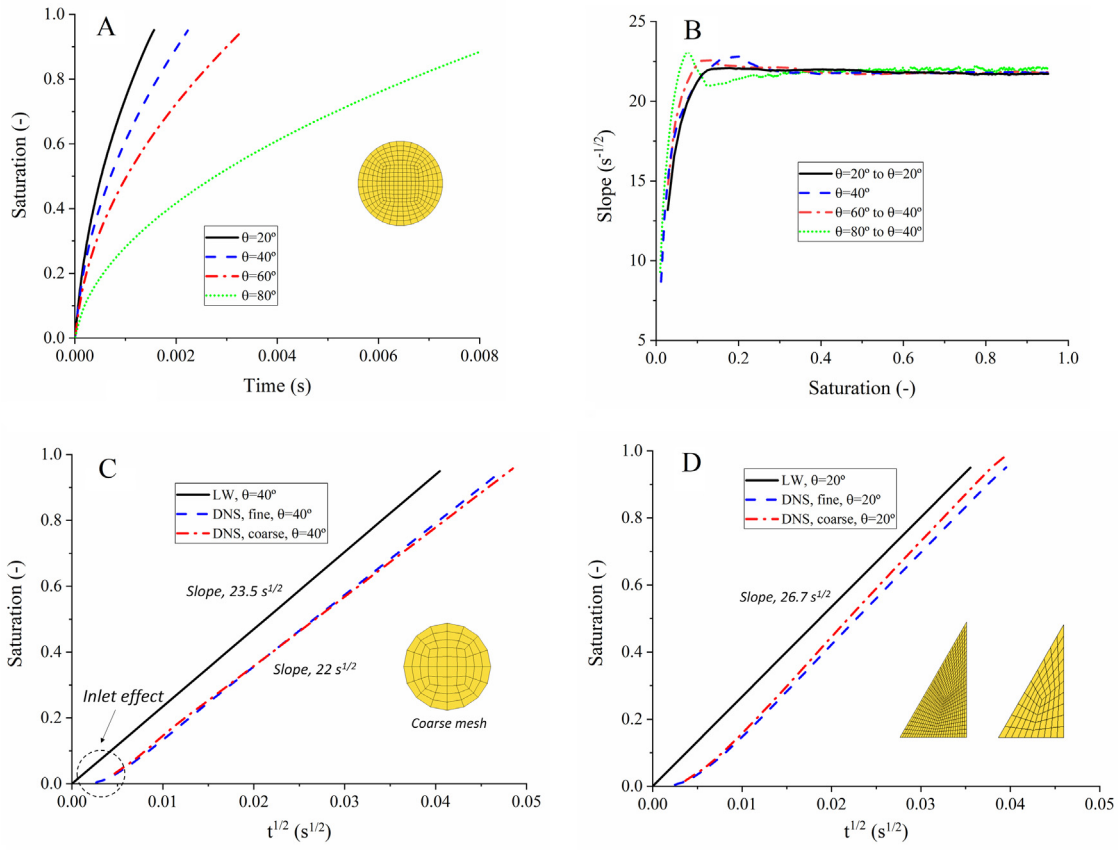

Fig. B1. Numerical studies of spontaneous imbibition of water into dry capillary tubes by the VOF model for the physical parameters and model settings in Table 1. (A) Spontaneous imbibition in a capillary tube of circular cross-section under different contact angle values. The radius of the cross-section is 20 μm, the tube length is 1 mm, and the inset shows the cross-sectional mesh, which is termed as 'fine mesh'. (B) The imbibition slope values versus saturation scaled by $\sqrt{\cos 40^0 / \cos\theta}$. (C) Comparison of the imbibition rates predicted by the Lucas-Washburn (LW) equation and the VOF model under the contact angle of 40°. The inset shows the coarse cross-sectional mesh. (D) Comparison of the imbibition rates predicted by the LW equation and the VOF model under the contact angle of 20° in a capillary tube of right triangular (one corner of 30°) cross-section. The inscribed radius is 20 μm, the tube length is 1 mm, and the inset shows the fine and coarse cross-sectional meshes.

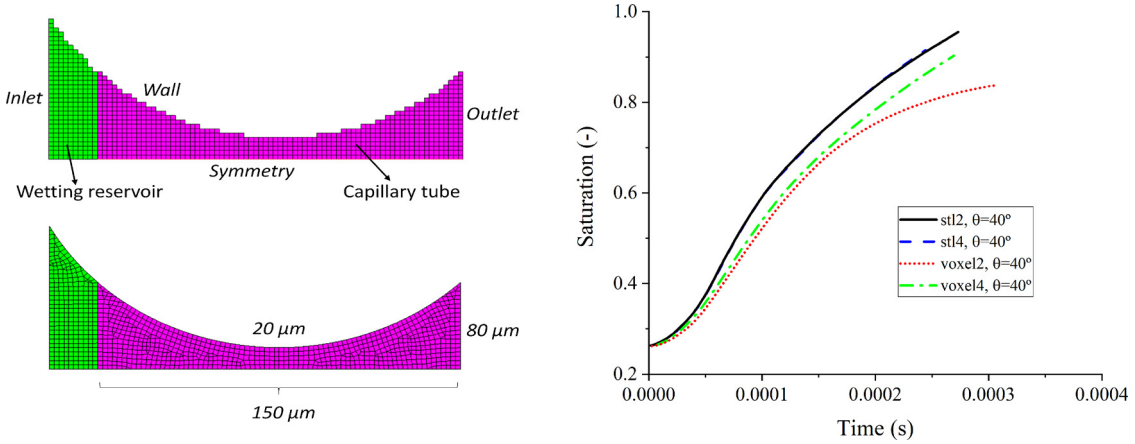

Fig. B2. (Left) Voxel representation and smooth representation (i.e., STL) of a 2D capillary tube and their associated computational meshes. (Right) Imbibition rates under two different meshing methods. The notation of 'stl4, θ=40' in the legend denotes the case study of the smooth-geometry representation with the contact angle of 40°. The mean element size is around 4 μm. The notation of 'voxel2, θ=40' in the legend indicates the case study of the voxel-representation with the contact angle of 40°. The voxel size is 2 μm.

mesh densities. First, it is seen that for the smooth-geometry representation the mesh size of 4 μm and 2 μm give the same imbibition rate, while for the voxel-representation reducing the mesh size of 4 μm to 2 μm gives slightly slower imbibition rate in the converging part of the tube, but much slower imbibition rate in the diverging part of the tube. We note that the refinement of the voxel-representation here is different from a higher voxel-resolution of the porous medium. The refinement here is conducted on the fixed voxel resolution of 4 μm. Second, with the same mesh density the VOF model predicts a faster imbibition process for the smooth-geometry representation than that for the voxel-representation. This is mainly due to the voxel-induced roughness of the wall, owing to the fact that a rough wall increases

the dissipation energy around three-phase contact lines (Forsberg et al., 2010).

Based on the above case studies of single capillary tubes, we may conclude that the mesh density with the voxel resolution of 25 μm is adequate for VOF simulations of spontaneous imbibition in the μCT scanning of sintered glass beads. A voxel-representation would slightly slow down the predicted imbibition rate in comparison to a smooth-representation. However, it can avoid the meshing of a complex porous medium.

Appendix C

Mass balance and capillary number in the pore-network simulations

Based on the constructed pore network, the discretized mass balance Eq. (3) is in the conservative form, which is solved by the first-order explicit scheme. To avoid extremely small time steps, at the end of each time step, we truncate the wetting saturation in a pore body as follows: when s_i^w is smaller than 10^{-6}, we set $s_i^w = 0$; when $(1 - s_i^w)$ is smaller than 10^{-6}, we set $s_i^w = 1$. This truncation practice may impact the mass imbalance. In our case studies, we calculate the mass imbalance of the wetting phase as:

$$\tilde{m}(t) = \left(\int_{t_0}^{t} \sum_{i=1}^{N} q_i^w - \sum_{i=1}^{N} V_i s_i^w \Big|_t \right) \Big/ \sum_{i=1}^{N} V_i \tag{C1}$$

where $\tilde{m}(t)$ is the mass imbalance at the imbibition time of t, q_i^w (m^3/s) is the net wetting flow rate of pore body i, and N is the number of pore bodies. Fig. C1 shows the wetting-phase mass imbalance in the pore-network modeling of spontaneous imbibition under different contact angle values and viscosity ratios. It is seen that for all case studies the mass imbalance is smaller than 10^{-3}, which is negligible. Furthermore, our case studies indicate that the truncation threshold has little impact on the mass imbalance.

Fig. C2 shows the temporal capillary number values in the pore-network modeling of spontaneous imbibition under different contact angle values and viscosity ratios. Obviously, for the air-water system, the capillary number decreases as the imbibition proceeds. At the viscosity ratio of unity, the capillary number keeps roughly constant before the wetting-phase breakthrough. At the viscosity ratio of 0.1, interestingly the capillary number also keeps roughly flat rather than increase, this is because the sharp wetting front does not hold any more (see Fig. 8B). Though the porous medium of sintered glass beads is highly permeable, for all case studies in this work the capillary number values are smaller than 10^{-3}. This indicates that the dynamic effect on the contact angle is minor.

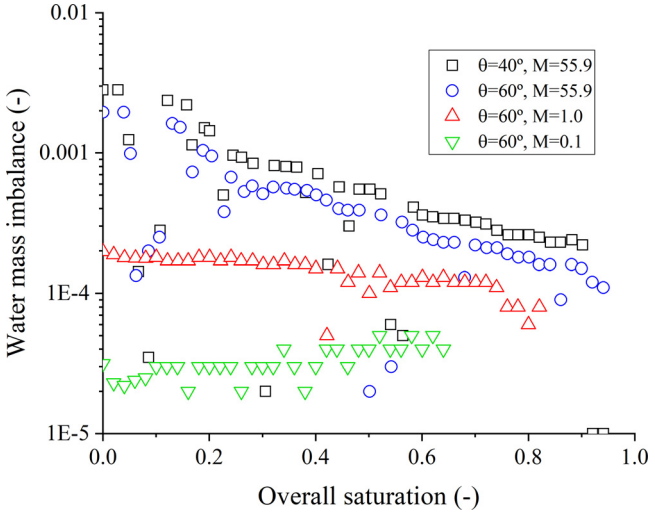

Fig. C1. Mass imbalance of the wetting phase in the pore-network modeling of spontaneous imbibition under different contact angle values and viscosity ratios.

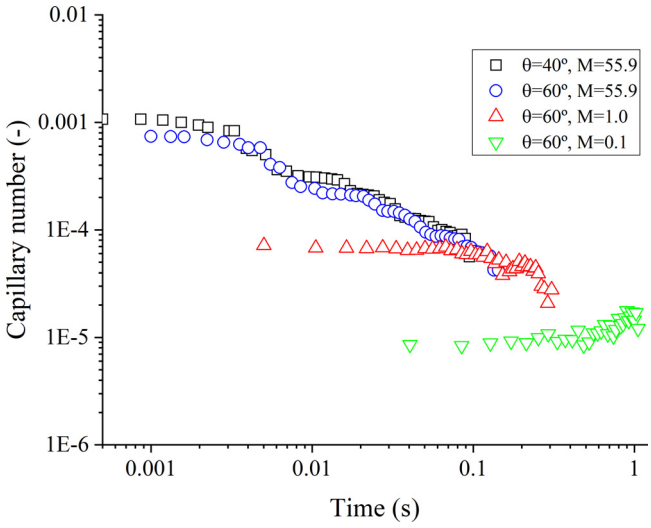

Fig. C2. Temporal capillary number values in the pore-network modeling of spontaneous imbibition under different contact angle values and viscosity ratios.

References

Aghaei, A., Piri, M., 2015. Direct pore-to-core up-scaling of displacement processes: Dynamic pore network modeling and experimentation. J. Hydrol. 522, 488–509. https://doi.org/10.1016/j.jhydrol.2015.01.004.

Aker, E., Måløy, K.J., Hansen, A., Batrouni, G.G., 1998. A two-dimensional network simulator for two-phase flow in porous media. Transp. Porous Media 32, 163–186. https://doi.org/10.1023/A:1006510106194.

Akin, S., Schembre, J.M., Bhat, S.K., Kovscek, A.R., 2000. Spontaneous imbibition characteristics of diatomite. J. Pet. Sci. Eng. 25, 149–165. https://doi.org/10.1016/S0920-4105(00)00010-3.

Alyafei, N., Al-Menhali, A., Blunt, M.J., 2016. Experimental and analytical investigation of spontaneous imbibition in water-wet carbonates. Transp. Porous Media 115, 189–207. https://doi.org/10.1007/s11242-016-0761-4.

Blunt, M.J., 1997. Pore level modeling of the effects of wettability. SPE J. https://doi.org/10.1093/oxfordjournals.afraf.a094799.

Brackbill, J.U., Kothe, D.B., Ridge, O., 1992. A Continuum Method for Modeling Surface Tension A Continuum Method for Modeling Surface Tension 9991. https://doi.org/10.1016/0021-9991(92)90240-Y.

Chen, L., Kang, Q., Mu, Y., He, Y.L., Tao, W.Q., 2014. A critical review of the pseudopotential multiphase lattice Boltzmann model: methods and applications. Int. J. Heat Mass Transf. 76, 210–236. https://doi.org/10.1016/j.ijheatmasstransfer.2014.04.032.

Chen, S., Qin, C., Guo, B., 2020. Fully implicit dynamic pore-network modeling of two-phase flow and phase change in porous media. Water Resour. Res. 56, 1–24. https://doi.org/10.1029/2020WR028510.

Zarandi, F., M.A., PillaiK.M., 2018. Spontaneous imbibition of liquid in glass fiber wicks, Part II: Validation of a diffuse-front model. AIChE J 64, 306–315. https://doi.org/10.1002/aic.15856.

Ferrari, A., Jimenez-Martinez, J., Le Borgne, T., Mèheust, Y., Lunati, I., 2015. Challenges inmodeling unstable two-phase flow experiments in porousmicromodels. Water Resour. Res. 51, 1381–1400. https://doi.org/10.1002/2014WR016384.Received.

Forsberg, P.S.H., Priest, C., Brinkmann, M., Sedev, R., Ralston, J., 2010. Contact line pinning on microstructured surfaces for liquids in the Wenzel state. Langmuir 26, 860–865. https://doi.org/10.1021/la902296d.

Gerke, K.M., Sizonenko, T.O., Karsanina, M.V., Lavrukhin, E.V., Abashkin, V.V., Korost, D.V., 2020. Improving watershed-based pore-network extraction method using maximum inscribed ball pore-body positioning. Adv. Water Resour. 140, 103576. https://doi.org/10.1016/j.advwatres.2020.103576.

Gostick, J.T., 2017. Versatile and efficient pore network extraction method using marker-based watershed segmentation. Phys. Rev. E 96, 1–15. https://doi.org/10.1103/PhysRevE.96.023307.

Gruener, S., Sadjadi, Z., Hermes, H.E., Kityk, A.V., Knorr, K., Egelhaaf, S.U., Rieger, H., Huber, P., 2012. Anomalous front broadening during spontaneous imbibition in a matrix with elongated pores. Proc. Natl. Acad. Sci. 109, 10245–10250. https://doi.org/10.1073/pnas.1119352109.

Guo, B., Bandilla, K.W., Nordbotten, J.M., Celia, M.A., Keilegavlen, E., Doster, F., 2016. A multiscale multilayer vertically integrated model with vertical dynamics for CO2 sequestration in layered geological formations. Water Resour. Res. https://doi.org/10.1002/2016WR018714.

Hefny, M., Qin, C., Saar, M.O., Ebigbo, A., 2020. Synchrotron-based pore-network modeling of two-phase flow in Nubian Sandstone and implications for cap-

illary trapping of carbon dioxide. Int. J. Greenh. Gas Control 103, 103164. https://doi.org/10.1016/j.ijggc.2020.103164.
Heshmati, M., Piri, M., 2014. Experimental investigation of dynamic contact angle and capillary rise in tubes with circular and noncircular cross sections. Langmuir 30, 14151–14162. https://doi.org/10.1021/la501724y.
Huang, X., Bandilla, K.W., Celia, M.A., 2016. Multi-physics pore-network modeling of two-phase shale matrix flows. Transp. Porous Media 111, 123–141. https://doi.org/10.1007/s11242-015-0584-8.
Hughes, R.G., Blunt, M.J., 2000. Pore Scale Modeling of Rate Effects in Imbibition. Transp. Porous Media 40, 295–322. https://doi.org/10.1023/A:1006629019153.
Jackson, M.D., Valvatne, P.H., Blunt, M.J., 2003. Prediction of wettability variation and its impact on flow using pore- to reservoir-scale simulations. J. Pet. Sci. Eng. 39, 231–246. https://doi.org/10.1016/S0920-4105(03)00065-2.
Joekar-niasar, V., Hassanizadeh, S.M., 2012. Pore-Network Modeling of Wicking: A Two-Phase Flow Approach, in: Masoodi Reza, P.K.M. (Ed.), . Taylor & Francis Group, pp. 237–262.
Joekar-Niasar, V., Hassanizadeh, S.M., Dahle, H.K., 2010. Non-equilibrium effects in capillarity and interfacial area in two-phase flow: dynamic pore-network modelling. J. Fluid Mech. 655, 38–71. https://doi.org/10.1017/S0022112010000704.
Kuijpers, C.J., Huinink, H.P., Tomozeiu, N., Erich, S.J.F., Adan, O.C.G., 2017. Sorption of water-glycerol mixtures in porous Al2O3 studied with NMR imaging. Chem. Eng. Sci. 173, 218–229. https://doi.org/10.1016/j.ces.2017.07.035.
Kunz, P., Zarikos, I.M., Karadimitriou, N.K., Huber, M., Nieken, U., Hassanizadeh, S.M., 2016. Study of multi-phase flow in porous media: comparison of sph simulations with micro-model experiments. Transp. Porous Media 114, 581–600. https://doi.org/10.1007/s11242-015-0599-1.
Li, J., McDougall, S.R., Sorbie, K.S., 2017. Dynamic pore-scale network model (PNM) of water imbibition in porous media. Adv. Water Resour. 107, 191–211. https://doi.org/10.1016/j.advwatres.2017.06.017.
Liu, Y., Cai, J., Sahimi, M., Qin, C., 2020. A study of the role of microfractures in countercurrent spontaneous imbibition by lattice boltzmann simulation. Transp. Porous Media 133, 313–332. https://doi.org/10.1007/s11242-020-01425-w.
Mason, G., Morrow, N.R., 2013. Developments in spontaneous imbibition and possibilities for future work. J. Pet. Sci. Eng. 110, 268–293. https://doi.org/10.1016/j.petrol.2013.08.018.
Mason, G., Morrow, N.R., 1991. Capillary behavior of a perfectly wetting liquid in irregular triangular tubes. J. Colloid Interface Sci. 141, 262–274. https://doi.org/10.1016/0021-9797(91)90321-X.
Mayer, R.P., Stowe, R.A., 1965. Mercury porosimetry-breakthrough pressure for penetration between packed spheres. J. Colloid Sci. https://doi.org/10.1016/0095-8522(65)90061-9.
Médici, E.F., Allen, J.S., 2013. Evaporation, two phase flow, and thermal transport in porous media with application to low-temperature fuel cells. Int. J. Heat Mass Transf. 65, 779–788. https://doi.org/10.1016/j.ijheatmasstransfer.2013.06.035.
Miao, X., Gerke, K.M., Sizonenko, T.O., 2017. A new way to parameterize hydraulic conductances of pore elements: a step towards creating pore-networks without pore shape simplifications. Adv. Water Resour. 105, 162–172. https://doi.org/10.1016/j.advwatres.2017.04.021.
Morrow, N.R., Mason, G., 2001. Recovery of oil by spontaneous imbibition. Curr. Opin. Colloid Interface Sci. 6, 321–337. https://doi.org/10.1016/S1359-0294(01)00100-5.
Nguyen, V.H., Sheppard, A.P., Knackstedt, M.A., Val Pinczewski, W., 2006. The effect of displacement rate on imbibition relative permeability and residual saturation. J. Pet. Sci. Eng. 52, 54–70. https://doi.org/10.1016/j.petrol.2006.03.020.
Patzek, T.W., 2001. Verification of a complete pore network simulator of drainage and imbibition. SPE J. 6, 144–156. https://doi.org/10.2118/71310-PA.
Patzek, T.W., Kristensen, J.G., 2001a. Shape factor correlations of hydraulic conductance in noncircular capillaries: I. One-phase creeping flow. J. Colloid Interface Sci. 236, 295–304. https://doi.org/10.1006/jcis.2000.7414.
Patzek, T.W., Kristensen, J.G., 2001b. Shape factor correlations of hydraulic conductance in noncircular capillaries: II. Two-phase creeping flow. J. Colloid Interface Sci. 236, 305–317. https://doi.org/10.1006/jcis.2000.7414.
Pavuluri, S., Doster, F., Maes, J., Yang, J., Regaieg, M., Moncorg, A., 2019. Towards pore network modelling of spontaneous imbibition : contact angle dependent invasion patterns and the occurrence of dynamic capillary barriers. Comput. Geosci..
Princen, H.M., 1970. Capillary phenomena in assemblies of parallel cylinders. III. Liquid Columns between horizontal parallel cylinders. J. Colloid Interface Sci. https://doi.org/10.1016/0021-9797(70)90167-0.
Qin, C.-Z., van Brummelen, H., 2019. A dynamic pore-network model for spontaneous imbibition in porous media. Adv. Water Resour. 133, 103420. https://doi.org/10.1016/j.advwatres.2019.103420.
Qin, C., 2015. Water transport in the gas diffusion layer of a polymer electrolyte fuel cell: dynamic pore-network modeling. J. Electrochem. Soc. 162, F1036–F1046. https://doi.org/10.1149/2.0861509jes.
Qin, C., Guo, B., Celia, M., Wu, R., 2019. Dynamic pore-network modeling of air-water flow through thin porous layers. Chem. Eng. Sci. 202, 194–207. https://doi.org/10.1016/j.ces.2019.03.038.
Rabbani, A., Ayatollahi, S., Kharrat, R., Dashti, N., 2016. Estimation of 3-D pore network coordination number of rocks from watershed segmentation of a single 2-D image. Adv. Water Resour. 94, 264–277. https://doi.org/10.1016/j.advwatres.2016.05.020.
Raeini, A.Q., Bijeljic, B., Blunt, M.J., 2015. Modelling capillary trapping using finite-volume simulation of two-phase flow directly on micro-CT images. Adv. Water Resour. 83, 102–110. https://doi.org/10.1016/j.advwatres.2015.05.008.
Raeini, A.Q., Blunt, M.J., Bijeljic, B., 2014. Direct simulations of two-phase flow on micro-CT images of porous media and upscaling of pore-scale forces. Adv. Water Resour. 74, 116–126. https://doi.org/10.1016/j.advwatres.2014.08.012.
Raeini, A.Q., Yang, J., Bondino, I., Bultreys, T., Blunt, M.J., Bijeljic, B., 2019. Validating the generalized pore network model using micro-CT images of two-phase flow. Transp. Porous Media 130, 405–424. https://doi.org/10.1007/s11242-019-01317-8.
Schembre, J., Kovscek, A.R., 1998. Spontaneous Imbibition in Low Permeability Media SUPRI TR 114 Rep.
Schmid, K.S., Alyafei, N., Geiger, S., Blunt, M.J., 2016. Analytical solutions for spontaneous imbibition: fractional-flow theory and experimental analysis. SPE J 21, 2308–2316. https://doi.org/10.2118/184393-pa.
Shams, M., Raeini, A.Q., Blunt, M.J., Bijeljic, B., 2018. A numerical model of two-phase flow at the micro-scale using the volume-of-fluid method. J. Comput. Phys. 357. https://doi.org/10.1016/j.jcp.2017.12.027.
Sheng, Q., Thompson, K., 2016. A unified pore-network algorithm for dynamic two-phase flow. Adv. Water Resour. 95, 92–108. https://doi.org/10.1016/j.advwatres.2015.12.010.
Shokrpour Roudbari, M., van Brummelen, E.H., Verhoosel, C.V., 2016. A multiscale diffuse-interface model for two-phase flow in porous media. Comput. Fluids 141, 212–222. https://doi.org/10.1016/j.compfluid.2016.07.006.
Sun, Y., Kharaghani, A., Tsotsas, E., 2016. Micro-model experiments and pore network simulations of liquid imbibition in porous media. Chem. Eng. Sci. 150, 41–53. https://doi.org/10.1016/j.ces.2016.04.055.
Sweijen, T., Nikooee, E., Hassanizadeh, S.M., Chareyre, B., 2016. The effects of swelling and porosity change on capillarity: DEM coupled with a pore-unit assembly method. Transp. Porous Media 113, 207–226. https://doi.org/10.1007/s11242-016-0689-8.
Hoang, T., Verhoosel, C.V., Qin, C., Auricchio, F., Reali, A., van Brummelen, H., 2018. Skeleton-stabilized ImmersoGeometric Analysis for incompressible viscous flow problems. Comput. Methods Appl. Mech. Eng. 344, 421–450. https://doi.org/10.1016/j.cma.2018.10.015.
Tartakovsky, A.M., Trask, N., Pan, K., Jones, B., Pan, W., Williams, J.R., 2016. Smoothed particle hydrodynamics and its applications for multiphase flow and reactive transport in porous media. Comput. Geosci. 20, 807–834. https://doi.org/10.1007/s10596-015-9468-9.
Thompson, K.E., 2002. Pore-scale modeling of fluid transport in disordered fibrous materials. AIChE J 48, 1369–1389. https://doi.org/10.1002/aic.690480703.
Tørå, G., Øren, P.E., Hansen, A., 2012. A dynamic network model for two-phase flow in porous media. Transp. Porous Media 92, 145–164. https://doi.org/10.1007/s11242-011-9895-6.
Valvatne, P.H., Blunt, M.J., 2004. Predictive pore-scale modeling of two-phase flow in mixed wet media. Water Resour. Res. 40, 1–21. https://doi.org/10.1029/2003WR002627.
Vizika, O., Avraam, D.G., Payatakes, A.C., 1994. On the role of the viscosity ratio during low-capillary-number forced imbibition in porous media. J. Colloid Interface Sci. 165, 386–401. https://doi.org/10.1006/jcis.1994.1243.
Wang, SenS., Feng, Q., Dong, Y., Han, X., Wang, ShouleiS., 2015. A dynamic pore-scale network model for two-phase imbibition. J. Nat. Gas Sci. Eng. 26, 118–129. https://doi.org/10.1016/j.jngse.2015.06.005.
Yang, J., Bondino, I., Regaieg, M., Moncorgé, A., 2017. Pore to pore validation of pore network modelling against micromodel experiment results. Comput. Geosci. 21, 849–862. https://doi.org/10.1007/s10596-017-9630-7.
Yang, Y., Li, Y., Yao, J., Zhang, K., Iglauer, S., Luquot, L., Wang, Z., 2019. Formation damage evaluation of a sandstone reservoir via pore-scale X-ray computed tomography analysis. J. Pet. Sci. Eng. 183, 106356. https://doi.org/10.1016/j.petrol.2019.106356.
Yin, X., Zarikos, I., Karadimitriou, N.K., Raoof, A., Hassanizadeh, S.M., 2019. Direct simulations of two-phase flow experiments of different geometry complexities using Volume-of-Fluid (VOF) method. Chem. Eng. Sci. 195, 820–827. https://doi.org/10.1016/j.ces.2018.10.029.
Yue, P., Feng, J.J., 2011. Wall energy relaxation in the Cahn-Hilliard model for moving contact lines. Phys. Fluids. https://doi.org/10.1063/1.3541806.
Zhao, B., MacMinn, C.W., Juanes, R., 2016. Wettability control on multiphase flow in patterned microfluidics. Proc. Natl. Acad. Sci. 113, 10251–10256. https://doi.org/10.1073/pnas.1603387113.
Zhao, B., MacMinn, C.W., Primkulov, B.K., Chen, Y., Valocchi, A.J., Zhao, J., Kang, Q., Bruning, K., McClure, J.E., Miller, C.T., Fakhari, A., Bolster, D., Hiller, T., Brinkmann, M., Cueto-Felgueroso, L., Cogswell, D.A., Verma, R., Prodanović, M., Maes, J., Geiger, S., Vassvik, M., Hansen, A., Segre, E., Holtzman, R., Yang, Z., Yuan, C., Chareyre, B., Juanes, R., 2019. Comprehensive comparison of pore-scale models for multiphase flow in porous media. Proc. Natl. Acad. Sci. 116, 13799–13806. https://doi.org/10.1073/pnas.1901619116.
Zhao, J., Qin, F., Derome, D., Carmeliet, J., 2020a. Simulation of quasi-static drainage displacement in porous media on pore-scale: Coupling lattice Boltzmann method and pore network model. J. Hydrol. 588, 125080. https://doi.org/10.1016/j.jhydrol.2020.125080.
Zhao, J., Qin, F., Derome, D., Kang, Q., Carmeliet, J., 2020b. Improved pore network models to simulate single-phase flow in porous media by coupling with lattice Boltzmann method. Adv. Water Resour. 145, 103738. https://doi.org/10.1016/j.advwatres.2020.103738.
Zheng, J., Ju, Y., Wang, M., 2018. Pore-scale modeling of spontaneous imbibition behavior in a complex shale porous structure by pseudopotential Lattice Boltzmann method. J. Geophys. Res. Solid Earth 123, 9586–9600. https://doi.org/10.1029/2018JB016430.
Zhuang, L., Hassanizadeh, S.M., Qin, C.-Z., de Waal, A., 2017. Experimental investigation of hysteretic dynamic capillarity effect in unsaturated flow. Water Resour. Res. 53, 9078–9088. https://doi.org/10.1002/2017WR020895.